

Experiments in Fluids manuscript No.  
(will be inserted by the editor)

Author accepted version. Final publication : Akutina, Y, Mydlarski, L.M., Gaskin, S. & Eiff, O. (2018) Error analysis of 3D-PTV through unsteady interfaces, Experiments in Fluids, 59(53): 1-19. doi:10.1007/s00348-018-2509-0

## Error analysis of 3D-PTV through unsteady interfaces

Y. Akutina<sup>1,2</sup>, L. Mydlarski<sup>3</sup>, S. Gaskin<sup>2</sup>, O. Eiff<sup>1</sup>

Received: date / Accepted: date

**Abstract** The feasibility of stereoscopic measurements through an unsteady optical interface is investigated. Position errors produced by a wavy optical surface are determined analytically, as are the optimal viewing angles of the cameras to minimize such errors. Two methods of measuring the resulting velocity errors are proposed. These methods are applied to 3D particle tracking velocimetry (3D-PTV) data obtained through the free surface of a water flow within a cavity adjacent to a shallow channel. The experiments were performed using two sets of conditions, one having no strong surface perturbations, and the other exhibiting surface gravity waves. In the latter case, the amplitude of the gravity waves was 6% of the water depth, resulting in water surface inclinations of about  $0.2^\circ$ . (The water depth is used herein as a relevant length scale because the measurements are performed in the entire water column. In a more general case, the relevant scale the maximum distance from the interface to the measurement plane,  $H$ , which here is the same as the water depth.) It was found that the contribution of the waves to the overall measurement error is low. The absolute position errors of the system were moderate (1.2% of  $H$ ). However, given that the velocity is calculated from the relative displacement of a particle between two frames, the errors in the measured water velocities were reasonably small because the error in the velocity is the relative position error over the average displacement distance. The relative position error was measured to be 0.04% of  $H$ , resulting in small velocity errors of 0.3% of the free-stream velocity (equivalent to 1.1% of the average velocity in the domain). It is concluded that even though the absolute positions to which the velocity vectors are assigned is distorted by the unsteady interface, the magnitude of the velocity vectors themselves remains accurate as long as the waves are slowly varying (have low curvature). The stronger the disturbances on the interface are (high amplitude, short wave length), the smaller is the distance from the interface at which the measurements can be performed.

**Keywords** 3D-PTV · error analysis · free-surface flows · unsteady optical interface · gravity waves

---

Yulia Akutina  
E-mail: yulia.akutina@kit.edu

<sup>1</sup> present address: Institute of Hydromechanics, Karlsruhe Institute of Technology, 76131 Karlsruhe, Germany.

<sup>2</sup> Department of Civil Engineering and Applied Mechanics, McGill University, Montréal, Canada.

<sup>3</sup> Department of Mechanical Engineering, McGill University, Montréal, Canada.

## 1 Introduction

Optical flow measurement techniques, based on tracking neutrally buoyant particles, have become more popular as increased computing power and camera capabilities now permit the collection of high-resolution data in both space and time. As a result, particle tracking velocimetry (PTV) and particle image velocimetry (PIV) have become important flow measurement techniques in research and other engineering applications. Both methods allow non-intrusive measurements of three velocity components in three dimensions, producing very large data sets. However, as these techniques become more elaborate and are also used in increasingly complex flows, measurement validation and error estimation become more difficult. Reliable validation techniques need to be developed for experiments with greater uncertainty, whose most common source is optical distortion. Although the ideal configuration for imaging is a planar surface or interface between the target and the cameras, in certain cases, the images must be obtained through an unsteady interface, *e.g.* in the presence of internal gravity waves in a stratified flow, through shock waves, or, as in the present case, through a free water surface with interfacial gravity waves (*e.g.* in rivers, oceans, lakes, *etc.*). Snell's Law can be used to calculate errors resulting from optical distortions due to disturbances at the water surface, and these errors increase linearly with distance from the interface. However, this does not necessarily imply that velocity errors are large, as they are determined from the relative displacement of particles over a time interval.

In this work, the use of optical velocimetry measurement systems is extended to an application with an unsteady interface arising from gravity waves. Two simple methods are developed to measure the associated velocity errors. Recommendations are made regarding the *i)* optimal camera angles with respect to the unsteady interface, and *ii)* maximum magnitude of the water surface disturbance so that the associated errors are negligible.

### 1.1 Error analysis techniques

In general, four different approaches can be used when undertaking an error analysis: *i)* benchmarking (*i.e.* performing a different experiment with a simple, well-known configuration); *ii)* comparison with another flow measurement technique; *iii)* analysis of all possible sources of error and their propagation into the final results; and *iv)* measurement of the error.

The first three methods require significant investments of time and/or additional experimental apparatus and/or equipment. In this work, we chose the approach number (*iv)* and attempt to develop universal and simple tests that estimate the total cumulative error of the final measured data. Previous work of this kind includes, for example, generating artificial particle clouds to estimate the total cumulative error of reproducibly simulated movement (either numerically or experimentally). For example, Fincham and Spedding (1997) glued particles onto a turntable with a prescribed angular velocity to calculate the systematic and random components of the uncertainty as a function of displacement. They also numerically simulated particles and analysed the error as a function of particle size, shape, brightness and seeding density. Alternatively, Weitbrecht et al (2002) quantified position errors by tracking particle clouds plotted on paper and mounted on a moving positioning system. Westerweel (2000) derived analytical expression for the sub-pixel displacement error in PIV and analysed it as a function of particle diameter and image density. Their results were also compared with PIV measurements performed on synthetic images. These works have resulted in very useful practical recommendations on how to choose particle diameters, seeding densities, and the time interval ( $\Delta t$ ) between image pairs. These methods are

well-suited to the investigation of the dependence of the error on certain parameters. However, as they do not reproduce the real flow field, they are not ideal for the evaluation of the absolute error for a particular experimental set-up. In addition, for the cases of flow with an unsteady optical interface, a traversing mechanism disturbs the interface, creating further complications. In a related study, Elsinga and Orlicz (2015) suggested a model for the estimation of position and velocity errors introduced by a shock wave in a compressible flow. Even though the effect of a shock wave is somewhat different, given that the medium has a variable refractive index, this work is the most relevant to the current set-up.

## 1.2 Measurements through an unsteady interface

Typically, PTV and PIV codes are capable of handling data obtained through an interface (or two) between media with different refractive indices (when light rays pass through three different media, *e.g.* air/glass/water), if all the interfaces are flat and stationary by either modelling the interfaces (ex. OpenPTV) or using higher order camera models. This allows, for example, imaging water flow through a plane glass wall accounting for refraction at the two interfaces (air/glass and glass/water). Additional methods have also been developed for specific cases of curved or unsteady interfaces, which has led to these two principal conclusions:

*i) It is possible to correct the distortions of an image if the exact shape of the interface is defined.* For example, Levin et al (2008) estimated the shape of the wavy water surface using an additional camera viewpoint at a low angle that imaged reflections off the surface. Morris and Kutulakos (2005) showed that one can reconstruct the shape of an interface by tracking a calibration pattern from two viewpoints. Richard and Raffel (2001) also suggested a method in which optical distortions of a background pattern were used to visualize the distortion field.

*ii) It is possible to reconstruct a still underwater image from an image sequence collected through surface waves.* Tian and Narasimhan (2009) recovered the shape of the water surface from an image sequence by fitting a spatial distortion model based on the wave equation.

However, if the shape of the interface is unknown a priori, and the imaging is not of a stationary scene behind the interface, but rather that of a dynamic flow field, no method exists to correct for the image distortions. We therefore investigate the magnitude of the ensuing error, or, alternatively, to what extent can waves be ignored when performing PIV or PTV through an unsteady interface.

## 2 Experimental setup

The data employed herein was obtained from experimental measurements designed to recreate the recirculating flow in a cavity<sup>1</sup> next to a shallow channel (Figure 1). The flume in which the experiments were performed had a 2 m long and 0.4 m wide straight section with a square 0.24 by 0.24 m<sup>2</sup> cavity at mid-channel. The bed was flat and the water depth,  $h$ , was 30 mm. Experiments were first performed with a free-stream velocity,  $U_\infty$ , of 0.19 m/s, resulting in a water-depth Reynolds number ( $Re = \frac{U_\infty h}{\nu}$ ) in the channel of 5400 and a Froude number ( $Fr = \frac{U_\infty}{\sqrt{g h}}$ ) of 0.33. At this free-stream velocity, a seiche<sup>2</sup> forms in the channel spanning the width of the channel and the cavity, resulting in a wavelength of

<sup>1</sup> Such a flow is also referred to as a bay or an embayment in different scientific communities.

<sup>2</sup> A shallow-water wave

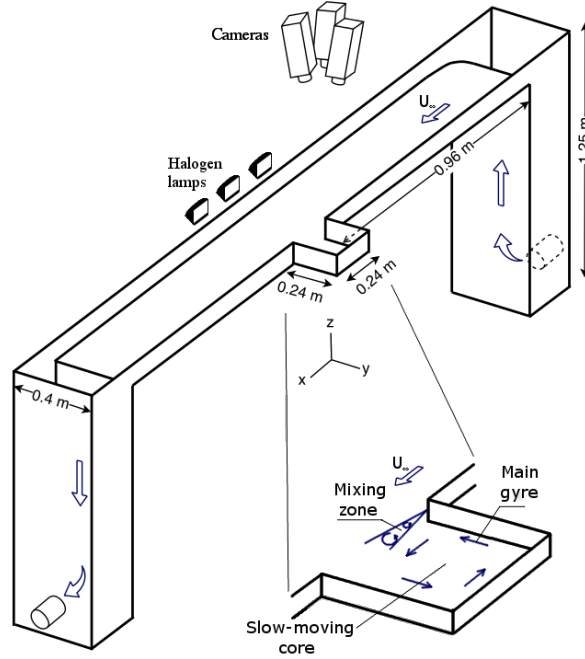


Fig. 1: Schematic of the experimental setup. Three cameras are mounted above the recirculating water channel, capturing the flow in a square cavity.

$2(0.24 \text{ m} + 0.40 \text{ m}) = 1.28 \text{ m}$ . The wave has an amplitude,  $\Delta z$ , of about 1 mm (or peak-to-peak amplitude of 2 mm) and frequency of 0.36 Hz (this data was obtained from the 3D-PTV measurements using the positions of the top particles in the measurement volume). The maximum surface angles,  $\beta$ , are about  $0.2^\circ$ , calculated using the half-wavelength of the seiche, 640 mm, and the amplitude of the wave, 2 mm, ( $= \tan^{-1}(2/640)$ ). A second set of experiments was also performed, for which the free-stream velocity was 0.13 m/s, such that there were almost no surface disturbances (water surface angles of  $0.02^\circ$  and wave amplitude 0.2 mm) – see Table 1.

3D-PTV was performed using three cameras mounted above the channel. Neutrally-buoyant polyethylene particles 212-250  $\mu\text{m}$  in diameter were seeded into the flow. Trajectories of the particles were simultaneously recorded with the three cameras at a rate of 600 frames per second. About 9,000 particles were identified and tracked at every frame. Their 3D positions and Lagrangian trajectories were obtained through spatial and temporal stereoscopic matching using the epipolar line intersection method. These calculations were performed using an open-source 3D-PTV software, that was initially developed at ETH Zurich (Willneff, 2003), and is supported today by the OpenPTV-Consortium (2014) (Gülan et al, 2012). The calculation of particle velocities was performed using centred differences with low-pass filtering using a moving polynomial fitted to 21 trajectory points (Lüthi et al, 2005). The reader is referred to Akutina (2016) for further

Table 1: Flow conditions

$U_\infty$ (m/s)	$h$ (m)	$Re_h$ , (-)	$Fr$ , (-)	$\Delta z$ , (mm)	$\beta^\circ$
0.19	0.03	5,400	0.33	1	0.2
0.13	0.03	3,900	0.24	0.2	0.02

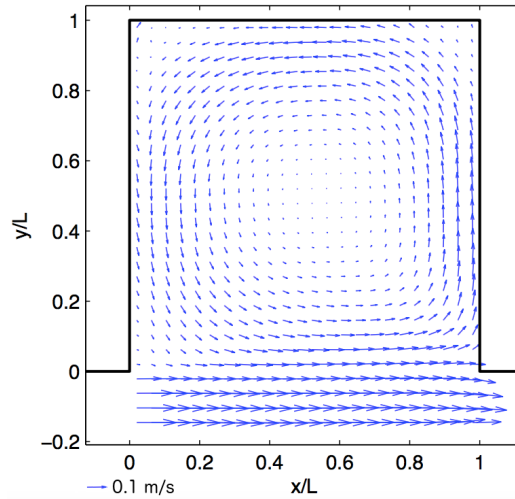


Fig. 2: Vector field of the horizontal time- and depth-averaged flow velocities for  $U_\infty = 0.19$  m/s. Top view of the cavity.  $L = 0.24$  m.

details of the experiment. The resulting time- and depth averaged flow field for the higher free-stream velocity is depicted in Figure 2. These velocities will be used in the estimation of the measurement errors.

### 3 Error analysis

Sources of uncertainty in laboratory measurements can be classified as either systematic or random errors. For time-averaged statistics, the contribution of the random components of the error to the overall uncertainty can be minimized by ensuring data sets are sufficiently long. However, for instantaneous data (*e.g.* measurements of the turbulence), the random component of the error must be quantified as well.

The sources of error in 3D-PTV are numerous as it is a multi-step procedure with errors associated with each stage of the underlying data acquisition and analysis. The first stage is the determination of the particle positions in the image space of each camera. Uneven lighting of the particles, imperfections in their geometry, digital noise in the cameras, and discretization noise all lead to errors in the determination of the position of the centre of mass of a particle.

In the second stage, the determination of particle correspondences between cameras relies on the mathematical model describing the relation between their image space and real space, accounting for the position of the cameras, refraction of the light rays going through the interface between different media (*e.g.* water, glass, air), lens distortion, *etc.* Parameters of this model are optimized during the calibration procedure, and its imperfections introduce bias into the data. Moreover, this model assumes a flat, stationary interface at the water surface, whereas the interface position (water surface elevation) varies in space and time in the present experiments. The unsteady interface significantly complicates this second stage of the analysis. First, there is a periodic error produced by the surface gravity waves. (This, and all other unsteady errors, are henceforth considered to be random errors, as their periodicity is not decomposed into different modes.) Second, there are small surface disturbances generated by Kelvin-Helmholtz vortical structures in the shear zone (Figure 1) between the cavity and the free stream. These disturbances result in a concave water surface, which, although small in amplitude, may have steeper surface angles than the gravity waves. Third, there is systematic error due to a concave water curvature

generated by the recirculating flow in the cavity. Assuming solid-body rotation and given the maximum rotation rate of the gyre for the current experiments, the free surface angle due to the centrifugal force can reach up to  $0.1^\circ$ .

In the third stage, particle trajectories are reconstructed from the three-dimensional positions of the particles in real space at multiple times. Uncertainty in this stage occurs due to ambiguity in the particle trajectory when paths cross or get too close. This is minimized by applying additional criteria based on a particle's characteristic velocity and acceleration from previous time steps. Malik et al (1993) state that if the ratio of the average particle spacing to the mean particle displacement during one time step is much greater than unity, then tracking is relatively easy and unambiguous. Velocities of the particles are calculated as first derivatives of a moving cubic spline fit to a particle trajectory, introducing a numerical error. Lastly, interpolation of the velocities onto a regular grid for time-averaging purposes is the final source of error.

It is difficult to estimate the contribution of each of the error sources described above, in addition to their propagation to the final cumulative error. We therefore circumvent this difficulty in the present work by analyzing test cases with known properties and statistics to directly estimate the total cumulative error. We then estimate the contributions of the different sources and find that the quality of the camera calibration and the refraction errors produced by surface oscillations play key roles.

Given that optical errors in a stereoscopic system are direct functions of camera viewing angles, it is necessary to make sure that the camera angles are optimally chosen for the current experiment before analysing error sources and relative contributions of different uncertainties. In Section 3.1, we present a theoretical analysis of position errors as a function of camera viewing angles. Optimum angles are determined as a function of the average surface disturbance. In Section 3.2, the errors introduced by the calibration of the cameras is estimated, emphasizing the importance of this procedure. In Section 3.3, we return to the errors introduced by the unsteady interface. Two methods are proposed to quantify the error in both position and velocity, but most importantly the latter. Finally, these methods are applied to the free-surface cavity flow.

### 3.1 Angle of the cameras with respect to the interface

In stereoscopic or tomographic measurements, it is widely accepted that the half-angle between the optical axes of the cameras should be greater than 30 degrees. Otherwise, the uncertainty normal to the imaging plane becomes considerably larger than that within the plane. To equally distribute the uncertainty in space, the half-angle between the cameras should be increased as much as possible, up to  $45^\circ$ . However, an unsteady optical interface (such as a free surface of water) introduces an additional factor that must be taken into account.

In a standard stereoscopic model, it is assumed that the optical interface is flat and stationary. However, when taking measurements through a wavy surface, this interface is not flat nor stationary as it exhibits changes in both curvature and height. Thus, a measurement error results from the difference between the model and reality. The error produced by surface perturbations has two components, the *i*) error due to the changing inclination of the interface, and *ii*) error due to its changing elevation. We begin by considering the effect of changes in the inclination of the interface. Using Snell's

law<sup>3</sup> we can relate the angle of incidence,  $\theta_1$ , and the angle of refraction,  $\theta_2$ , of the light rays travelling from a particle to one of the cameras as:

$$\frac{\sin \theta_1}{\sin \theta_2} = \frac{n_2}{n_1} = c, \quad (1)$$

$$\theta_1 = \sin^{-1}(c \sin \theta_2), \quad (2)$$

where  $n$  is the refractive index of the respective media and  $c$  is the ratio of refractive indices. However, if the interface is tilted by an angle  $\beta$ , there will be an error in the predicted values  $\theta_1$  (Figure 3). The real angle will be equal to:

$$\theta_{1,real} = \sin^{-1}[c \sin(\theta_2 - \beta)] + \beta, \quad (3)$$

and the angular error produced by the surface tilt,  $\Delta\theta$ , can be written as the difference ( $\theta_1 - \theta_{1,real}$ ):

$$\Delta\theta = \sin^{-1}(c \sin \theta_2) - \sin^{-1}[c \sin(\theta_2 - \beta)] - \beta. \quad (4)$$

This relationship is illustrated in Figure 4. It is evident that for relatively small camera angles ( $\theta_2 < 10^\circ$ ) the error is almost independent of  $\theta_2$  and grows linearly with the surface slope,  $\beta$ .

The position error resulting from the inclination of the surface is proportional to the distance of a particle from the interface. Thus, to calculate the maximum horizontal position error,  $E_\beta$ , one should use the maximum distance from the interface,  $H$ , (here, the same as the water depth):

$$E_\beta = H(\tan \theta_1 - \tan \theta_{1,real}), \quad (5)$$

Next, we consider the effect of a change in the elevation of the surface. Figure 5 depicts a schematic of a light ray going

<sup>3</sup> Snell's law is valid for low-curvature interfaces with a wavelength larger than the wavelength of the light. In the case of a wavy water surface, this condition is easily satisfied.

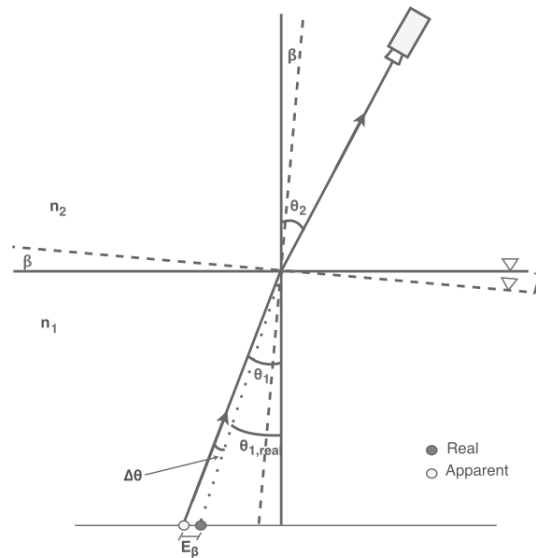


Fig. 3: Schematic of the horizontal position error,  $E_\beta$  produced by an inclined water surface.

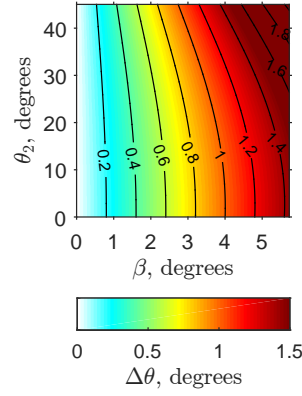


Fig. 4: Error due to the slope of the interface,  $\Delta\theta$ , in degrees.

through the interface elevated by a distance  $\Delta z$ . Trigonometry leads to the following expression for the resulting position error,  $E_{\Delta z}$ :

$$E_{\Delta z} = \Delta z [\tan \theta_2 - \tan \theta_1]. \quad (6)$$

Unlike  $E_\beta$ , the error  $E_{\Delta z}$  grows both with the camera angle and with the elevation of the surface (Figure 6). The total horizontal error,  $E_h$ , produced by the surface perturbations  $E_\beta$  and  $E_{\Delta z}$  is:

$$E_h = \sqrt{E_\beta^2 + E_{\Delta z}^2}, \quad (7)$$

which is smaller for lower camera angle<sup>4</sup>. However, it is well-established that a lower camera angle results in a higher out-of-plane uncertainty due to stereoscopy (out-of-plane here is considered to be the vertical direction). Thus, it is

<sup>4</sup> The errors due to the slope and height of the interface are considered here to be uncorrelated due to different wave types. For example, the sloshing waves (herein) have very low slopes, but a rather noticeable amplitude, whereas capillary waves have very small amplitude and steep slopes. Also, if one considers a single type of wave (imagine a sinus function), the points with the highest  $\Delta z$  have zero slope and *vice versa*. It is, therefore, possible that these effects are somewhat negatively correlated and thus, taking their root square sum may only overestimate the error.

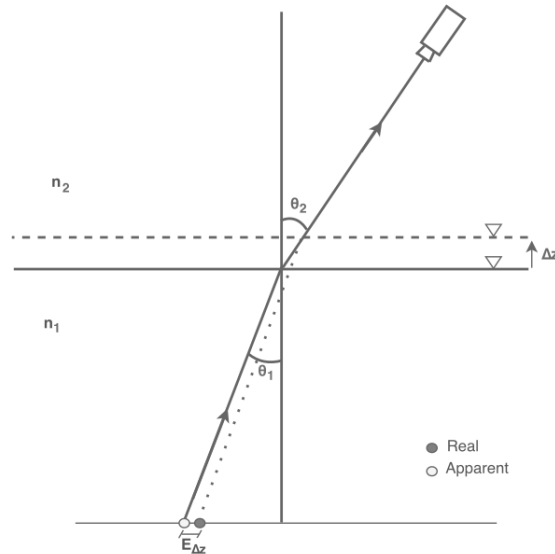


Fig. 5: Schematic of the horizontal position error,  $E_{\Delta z}$ , produced by an elevated water surface.

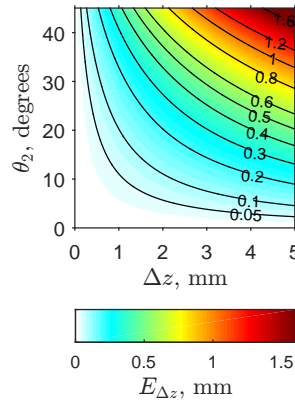


Fig. 6: Horizontal position error due to the surface elevation.

necessary to optimize the camera angle to minimize both effects. The distortions due to the waves, taking into account the stereoscopic configuration, are depicted on Figure 7. Sketch *a* shows how different combinations of surface inclinations for two cameras result in different position errors. When inclination is the same, the apparent particle position (empty circle) is lower or higher than the true position (solid circle). When the slope is different for the two cameras, the position error is horizontal. A similar result is shown on sketch *b*, where different combinations of surface elevations for the two cameras also result in the area of uncertainty in the form of a rhombus. In both cases, *a* and *b*, the relationship between the vertical and horizontal position errors can be approximated as:

$$E_v = \frac{E_h}{\tan\theta_1} = \frac{\sqrt{E_\beta^2 + E_{\Delta z}^2}}{\tan\theta_1} \tag{8}$$

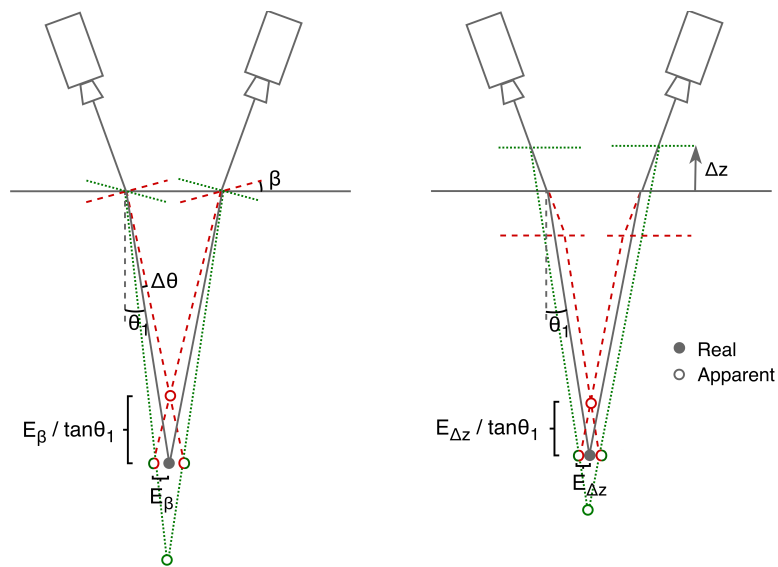


Fig. 7: Relationship between the vertical and horizontal position errors in a stereoscopic system for *a*) different combinations of surface inclination, and *b*) for different combinations of surface elevations.

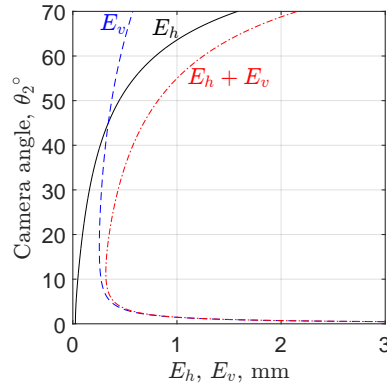


Fig. 8: Horizontal,  $E_h$ , vertical,  $E_v$ , and total,  $E_h + E_v$ , error produced by the surface oscillations in the present study, for the distance from the interface,  $H = 0.03$  m, the maximum surface elevation  $\Delta z = 1$  mm, and surface slope  $\beta = 0.2^\circ$ .

### 3.1.1 Errors in the present experiment

For the experiments herein, the maximum amplitude of the surface waves is about 1 mm and the resulting surface angle is  $\sim 0.2^\circ$ . Figure 8 presents the horizontal and vertical errors as a function of the camera angle for these disturbances. The vertical error grows rapidly with decreasing camera angles,  $\theta_2$ , below  $7^\circ$ . The horizontal error increases slowly (approximately linearly) with  $\theta_2$  for angles less than  $30^\circ$  and more rapidly thereafter. The two graphs cross at the angle of  $45^\circ$ , where the vertical and horizontal errors are equal. The selected camera angle should minimize  $E_h + E_v$ . For the current experiments, camera angles of about  $7.5^\circ$  were measured from the calibration procedure. The corresponding position errors for this angle are about 0.04 mm in the horizontal direction and 0.3 mm in vertical (which corresponds well with the measured position errors obtained in the next sections, 0.1 and 0.3 mm, respectively).

### 3.1.2 Guideline: How to choose the camera angle in the case of an unsteady interface

The optimum camera angle is that which results in the minimum value of  $E_h + E_v$ , which depends upon: the slope of the interface  $\beta$ , its change in elevation  $\Delta z$ , and the depth of the flow  $H$ . The trends in the variation of the optimum camera angle,  $E_h$  and  $E_v$  are presented by keeping  $H$  constant (and equal to 30 and 100 mm) and varying the other two independent variables over physically relevant parameter ranges ( $\beta = 0 - 3.5^\circ$ ,  $\Delta z = 0 - 4$  mm). Figures 9 a and d depict the optimum camera angles and the corresponding horizontal (b, e) and vertical (c, f) errors for the two fixed flow depths. It is clear that for small depths, the optimum camera angle is more sensitive to the combination of parameters  $\beta$  and  $\Delta z$ , while for deeper flows, the error (both vertical and horizontal) becomes almost a linear function of the surface slope. Considering all these conditions, the optimum camera angle,  $\theta_2$ , lies between  $6^\circ$  and  $32^\circ$  for different wave properties. Should it be required, the error magnitudes for specific cases, can be calculated using equations (5) to (8).

In the next sections, the errors introduced during the calibration procedure will be compared with errors due to the surface waves. Then, velocity errors will be calculated based on the position errors and the particular flow field.

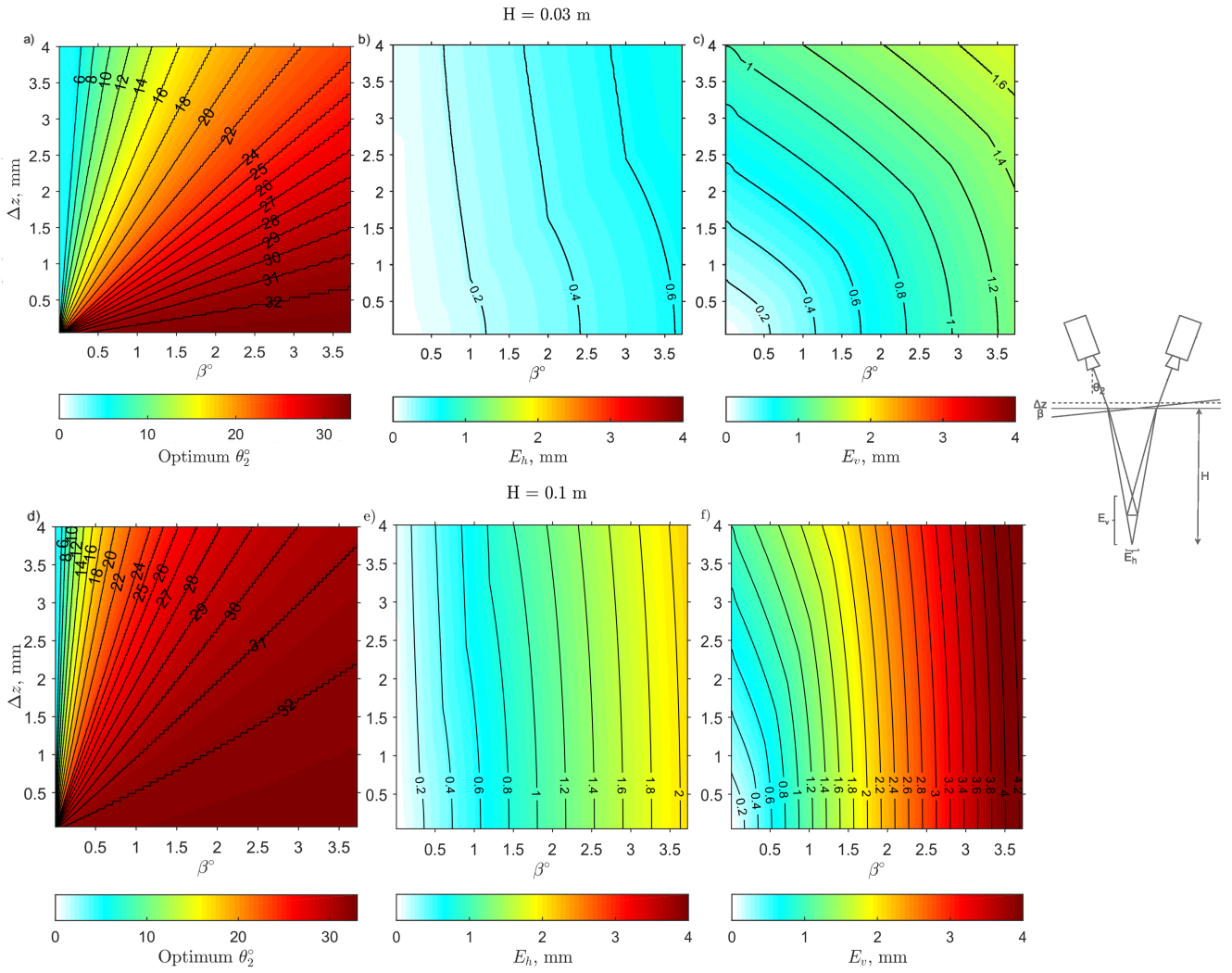


Fig. 9: *a), d)* Optimum angle of the cameras ( $\theta_2$ ) in a stereoscopic or a tomographic system as a function of the slope ( $\beta$ ) and change in elevation ( $\Delta z$ ) of an unsteady optical interface (*i.e.* free water surface). *b), e)* and *c), f)* respectively correspond to the horizontal ( $E_h$ ) and vertical ( $E_v$ ) errors produced by this variable interface, given that the optimum angle is used. Depth of the measurement volume  $H = 0.03$  m (*a, b, c*) and 0.1 m (*d, e, f*).

### 3.2 Calibration of the cameras

Before making stereo or tomographic measurements with a set of cameras, a camera calibration is undertaken to determine the exact positions and angles of the cameras in addition to their optical parameters, such as lens distortion. The calibration consists of an optimization procedure in which these geometric parameters are found using fixed data points on a calibration object of known geometry (Figure 10) (Maas et al, 1993). However, the result of the optimization is never perfect and introduces a systematic error. To estimate this error, the stereo-matching algorithm is run on the calibration object using the new parameters and the calculated positions are compared with the true ones.

The calibration object shape was selected to provide data points within the full 3D volume to be studied without the need for calibration at different flow depths. Points were machined on the calibration object with a diameter of 0.3 mm with a position accuracy of 0.03 mm. The systematic error introduced by the calibration is determined by comparing the true and calculated (post calibration) position of the points on the calibration object, as shown in Figure 11. The



Fig. 10: Calibration object of known geometry used to determine the position of the cameras relative to the measurement domain (defined by 1104 holes 0.3 mm in diameter positioned with the precision of  $\pm 0.03$  mm and filled with white silicone) (Akutina, 2016).

r.m.s. values of the error distributions are 0.03 mm, 0.03 mm and 0.20 mm in the  $x$ -,  $y$ - and  $z$ -directions, respectively. In most locations the  $x$  and  $y$  errors are below the machining precision and the error in  $z$  is below the machining precision divided by  $\tan \theta_2$  (about 0.3 mm), where  $\theta_2$  is the angle of the cameras (see Section 3.1). However, near the edges of the measurement domain, the error can reach 0.15 mm in the horizontal directions and 1 mm in the vertical direction.

It is important to note that the calibration procedure was performed in still water as the calibration object would disturb the flow rendering the calibration invalid. Thus, the calculated position errors do not account for the effects of the unsteady interface.

### 3.3 Estimating cumulative errors in position and velocity

Once the cameras are placed with the optimal angle (as per Section 3.1.1) and an approximate estimation of the position errors due to the unsteady interface and calibration are obtained, an estimation of the cumulative position error of the whole procedure and the resulting velocity error is required.

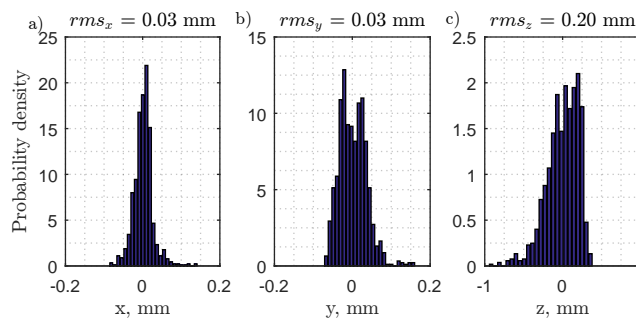


Fig. 11: Discrete probability density functions (PDFs) of the position error in the  $x$ ,  $y$ , and  $z$ -directions ( $a$ ,  $b$ , and  $c$  respectively). The error is measured in the still water by comparing the true and calculated positions of the dots on the calibration object.

Two methods were developed to assess the total measurement errors. In Method 1, a flat thin pane of glass with a precise pattern of dots was placed at the bottom of the flow. The flow disturbances introduced are negligible, so the total position error including the influence of the surface waves can be assessed (at the bed where the position error will be maximal). The velocity error is then calculated from the spatial gradient of the position error, similarly to the approach of Elsinga and Orlicz (2015).

In Method 2, a so-called “dumbbell” (a little rod with two particles glued onto it) is moved around in the flow. The relative velocity of the two particles along the vector connecting them must be zero, thus providing a way to measure velocity error in the experiments. These two methods and their application are described in the following two subsections.

### 3.3.1 Velocity errors - Method 1: Dot pattern

Assume there are a number of fixed points with known geometrical positions within the measurement domain. These points can be tracked in time by the PTV/PIV system. In every frame, the measured positions,  $\mathbf{r}_m(x, y, t)$ , of every point are extracted and compared with their true position,  $\mathbf{r}(x, y)$ . A position error vector,  $\mathbf{r}'$ , associated with every point, for every frame in the test, is then obtained:

$$\mathbf{r}'(x, y, t) = \mathbf{r}_m(x, y, t) - \mathbf{r}(x, y). \quad (9)$$

The total error can be divided into systematic and random components, referred to as  $\mathbf{r}'_s$  and  $\mathbf{r}'_r$ . Taking the time average of  $\mathbf{r}'(x, y, t)$  yields the systematic error of the position estimate for every point in the pattern:

$$\mathbf{r}'_s(x, y) = \frac{1}{N} \sum_{i=1}^N \mathbf{r}'(x, y, t_i), \quad (10)$$

where  $T = N\Delta t$  is the duration of the data set. The standard deviation of  $\mathbf{r}'(x, y, t)$  quantifies the random component of the position error:

$$\mathbf{r}'_r(x, y) = \sqrt{(\mathbf{r}'(x, y, t) - \mathbf{r}'_s(x, y))^2}. \quad (11)$$

The measured velocity of a particle,  $\mathbf{u}_m$ , is the difference in its measured position,  $\mathbf{r}_m$ , over the time interval,  $\Delta t$ , between two frames. Given that the measured position is the true position,  $\mathbf{r}$ , plus the position error,  $\mathbf{r}'$ , an expression for the measured velocity can be derived:

$$\mathbf{u}_m = \frac{(\mathbf{r}(\mathbf{x}_2) + \mathbf{r}'(\mathbf{x}_2)) - (\mathbf{r}(\mathbf{x}_1) + \mathbf{r}'(\mathbf{x}_1))}{\Delta t} = \mathbf{u} + \mathbf{u}', \quad (12)$$

where  $\mathbf{u}$  is the particle's true velocity. The error in velocity,  $\mathbf{u}'$ , is therefore:

$$\mathbf{u}' = \frac{\mathbf{r}'(\mathbf{x}_2) - \mathbf{r}'(\mathbf{x}_1)}{\Delta t}, \quad (13)$$

*i.e.*, proportional to the difference in the errors in the position vectors. Note that, if the position error was the same everywhere, there would be no error in the velocity. The gradient in the position error over the volume of interest is

estimated using a Taylor series expansion (hereafter switching from vector to index notation for clarity):

$$r'_i((x_2)_i) = r'_i((x_1)_i) + \sum_j \frac{\partial r'_i}{\partial x_j} ((x_2)_j - (x_1)_j) + \dots \quad (14)$$

where  $i = 1, 2, 3$  and  $j = 1, 2, 3$ . (Note: Einstein summation convention is not implied here.) Substituting (14) into (13) and neglecting higher order terms, one obtains:

$$u'_i \approx \frac{\partial r'_i}{\partial x_j} \frac{(x_2)_j - (x_1)_j}{\Delta t} = \frac{\partial r'_i}{\partial x_j} u_j \quad (15)$$

Thus, the velocity error at a point can be estimated by the gradient of the position error multiplied by the particle's velocity. Dividing both sides by velocity, we obtain an expression for the relative velocity error:

$$\frac{u'_i}{u_i} = \sum_j \frac{\partial r'_i}{\partial x_j} \frac{u_j}{u_i}. \quad (16)$$

For an isotropic flow  $\frac{u_j}{u_i} \approx 1$ , so an approximate criterion for the quality of velocity measurements in a relatively isotropic flow can be given by specifying that  $\frac{\partial r'_i}{\partial x_j}$  be less than a critical value (say, 5%) everywhere. If the flow has regions of strong shear, as in the present case, the ratio  $\frac{u_j}{u_i}$  will vary in space and should be included in the calculation to render this error estimate more accurate. As undertaking this task for the instantaneous data is excessive, the time-averaged velocity field is used to characterise the anisotropy. Doing so, the relative velocity error can then be expressed as:

$$\frac{u'_i}{\bar{u}_i} = \begin{pmatrix} \frac{\partial}{\partial x} (r'_x) + \frac{\partial}{\partial y} (r'_x) \frac{\bar{u}_y}{\bar{u}_x} + \frac{\partial}{\partial z} (r'_x) \frac{\bar{u}_z}{\bar{u}_x} \\ \frac{\partial}{\partial x} (r'_y) \frac{\bar{u}_x}{\bar{u}_y} + \frac{\partial}{\partial y} (r'_y) + \frac{\partial}{\partial z} (r'_y) \frac{\bar{u}_z}{\bar{u}_y} \\ \frac{\partial}{\partial x} (r'_z) \frac{\bar{u}_x}{\bar{u}_z} + \frac{\partial}{\partial y} (r'_z) \frac{\bar{u}_y}{\bar{u}_z} + \frac{\partial}{\partial z} (r'_z) \end{pmatrix}. \quad (17)$$

In Method 1, the calibration object is two-dimensional, providing only horizontal derivatives of the position error field. Thus, the  $\frac{\partial}{\partial z} r'_i$  components are unknown. However, given that  $\frac{\bar{u}_z}{\bar{u}_x}$  or  $\frac{\bar{u}_z}{\bar{u}_y}$  are small in the current experiment (as the vertical velocity is an order of magnitude smaller than the horizontal ones), these terms can be justifiably neglected. Thus, the final approximation for the absolute velocity error in Method 1 is:

$$\begin{aligned} u'_x &= \frac{\partial r'_x}{\partial x} \bar{u}_x + \frac{\partial r'_x}{\partial y} \bar{u}_y \\ u'_y &= \frac{\partial r'_y}{\partial x} \bar{u}_x + \frac{\partial r'_y}{\partial y} \bar{u}_y \\ u'_z &= \frac{\partial r'_z}{\partial x} \bar{u}_x + \frac{\partial r'_z}{\partial y} \bar{u}_y. \end{aligned} \quad (18)$$

Performing these operations on the systematic ( $\mathbf{r}'_s$ ) and random ( $\mathbf{r}'_r$ ) components of the position error vectors, one obtains the systematic ( $\mathbf{u}'_s$ ) and random ( $\mathbf{u}'_r$ ) components of the velocity error:

$$(u'_s)_i = \sum_{j=1}^2 \frac{\partial (r'_s)_i}{\partial x_j} \bar{u}_j, \quad (19)$$

$$(u'_r)_i = \sum_{j=1}^2 \frac{\partial (r'_r)_i}{\partial x_j} \bar{u}_j, \quad (20)$$

where  $i = 1, 2, 3$  and  $j = 1, 2$ .

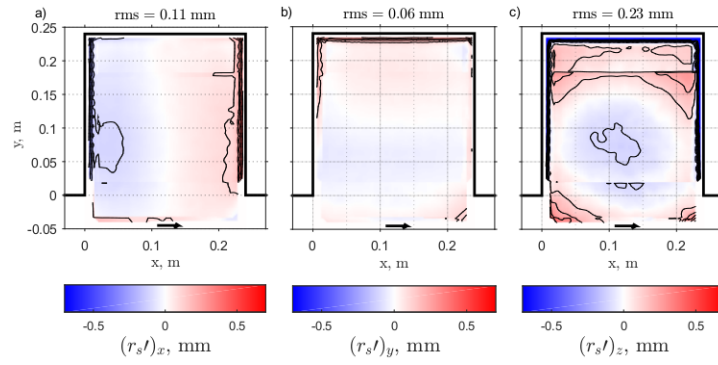


Fig. 12: Systematic position error,  $\mathbf{r}'_s$ , in  $x$ ,  $y$ , and  $z$ -directions (plots  $a$ ,  $b$ , and  $c$ , respectively) for the lower free-stream velocity,  $U_\infty = 0.13$  m/s. Isocontour lines are plotted in 0.1 mm increments.

This method was implemented using a Cartesian pattern of 512 equally-spaced white dots, 0.3 mm in diameter, printed on black background on 228 mm by 228 mm by 0.56 mm thick pane of extra rigid “Gorilla” glass. The glass pane was placed on the bottom of the cavity and tests were run at the two free-stream velocities of ( $U_\infty = 0.13$  and 0.19 m/s). The position errors converged after 10 s (6000 images) for positions within the cavity and after 30 s (18000 images) in the mixing layer, which is the most turbulent region of the flow.

Having acquired the series of images of the dots on the bottom of the flow, the position errors were determined using equations (10) and (11). Figure 12 presents the systematic position error field in  $x$ -,  $y$ -, and  $z$ -directions for the lower free-stream velocity. It is clear from the graphs that the error is the largest near the walls of the cavity (up to 0.7 mm), presumably due to capillary action increasing the surface slope at these near-wall locations. The systematic error in the rest of the cavity is mostly below 0.1 mm. A small increase in the position error ( $< 0.2$  mm) occurs in Figure 12c, due to the edge of the glass pane creating a minor flow disturbance. (Note: the calculation of the systematic error can also be affected by imperfections of the pattern of the dots, of the glass pane, or local flow disturbances generated by the glass edges, whereas the random component is a fluctuation around the mean, and hence, unaffected by these factors.)

Figures 13 and 14 present the random component of the position error for the lower free-stream velocity (with no gravity waves) and the higher one (with gravity waves), respectively. In all but one of the cases, for the vertical error at higher free-stream velocity, the random error,  $\mathbf{r}'_r$ , is significantly smaller than the systematic one,  $\mathbf{r}'_s$ , (see Table 2). Since

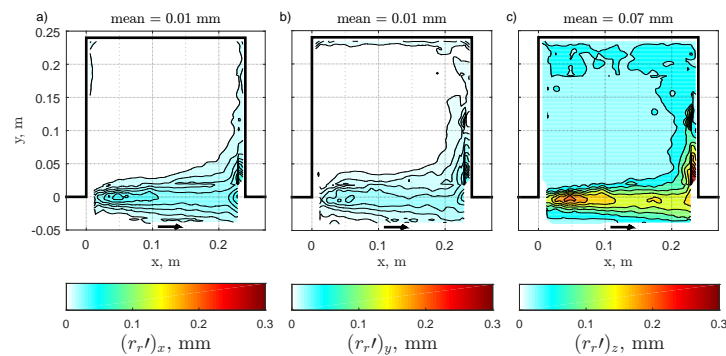


Fig. 13: Random position error,  $\mathbf{r}'_r$ , in the  $x$ ,  $y$ , and  $z$ -directions (plots  $a$ ,  $b$ , and  $c$ , respectively) for the lower free-stream velocity,  $U_\infty = 0.13$  m/s. Isocontour lines are plotted in 0.03 mm increments.

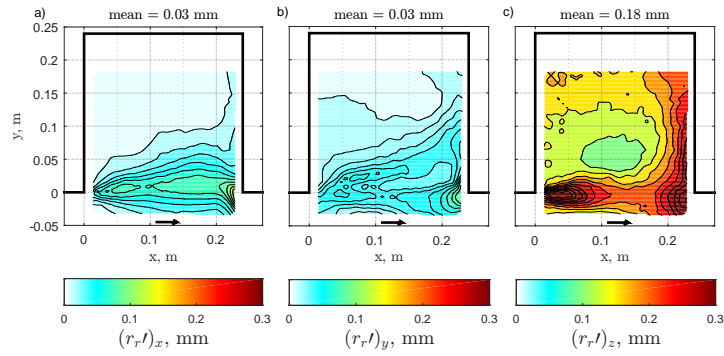


Fig. 14: Random position error,  $\mathbf{r}'_r$ , in the  $x$ ,  $y$ , and  $z$ -directions (plots  $a$ ,  $b$ , and  $c$ , respectively) for the higher free-stream velocity,  $U_\infty = 0.19$  m/s. Isocontour lines are plotted in 0.03 mm increments.

the effect of unsteady surface disturbances is reflected only in the random component, it appears that surface disturbances are not the most important error source in these measurements. Another important observation is that the smaller scale Kelvin-Helmholtz vortices in the shear layer created steeper surface slopes, and therefore larger position errors, than the surface gravity waves with the 2 mm peak-to-peak amplitude.

The propagation of the position errors into the velocity calculation of a moving particle is then computed using equations (19) and (20), where the spatial derivatives of  $\mathbf{r}'_s$  and  $\mathbf{r}'_r$  were approximated using a central difference scheme.

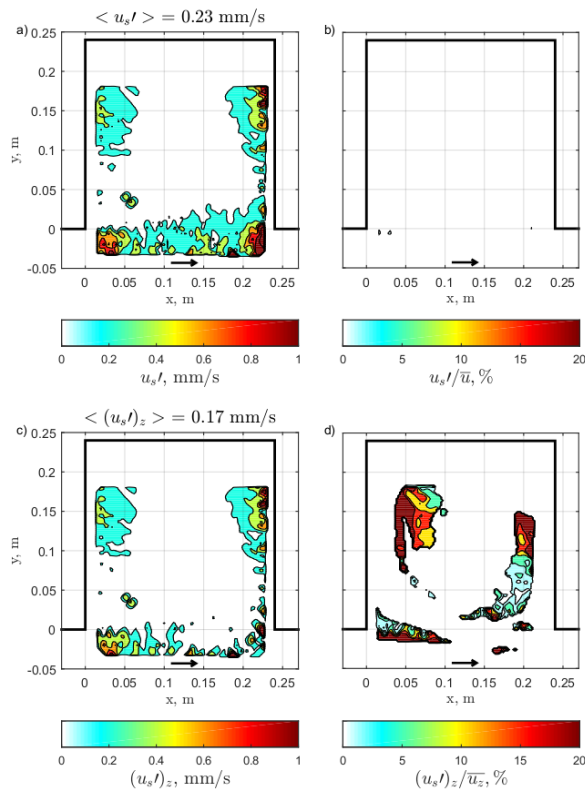


Fig. 15: *First row*: Systematic velocity error,  $u'_s$ ,  $a$ ) absolute value,  $b$ ) relative to the local velocity. *Second row*: Vertical component of the systematic velocity error,  $(u'_s)_z$ ,  $c$ ) absolute value,  $d$ ) relative to the local vertical velocity.  $U_\infty = 0.19$  m/s.

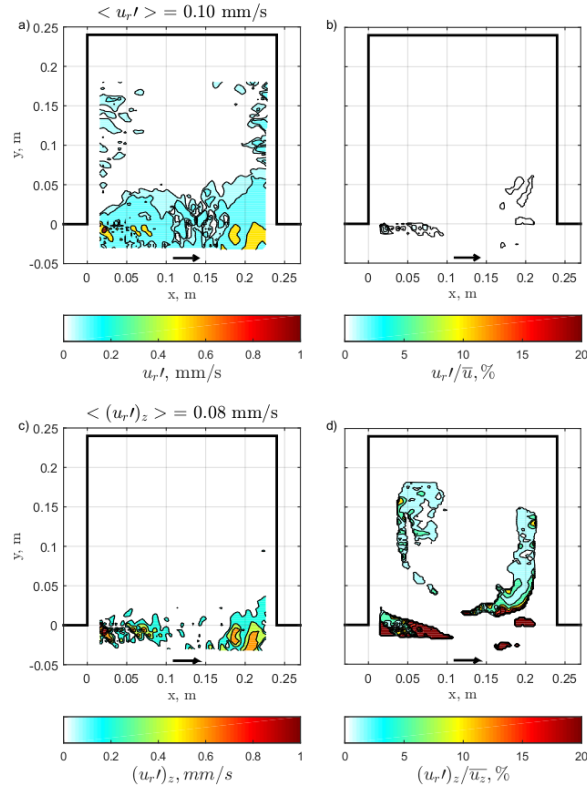


Fig. 16: *First row*: Random velocity error,  $u'_r$ , *a*) absolute value, *b*) relative to the local velocity. *Second row*: Vertical component of the random velocity error,  $(u'_r)_z$ , *c*) absolute value, *d*) relative to the local vertical velocity.  $U_\infty = 0.19 \text{ m/s}$ .

The detailed analysis is presented only for the higher free-stream velocity case with the gravity waves. Specifically, Figures 15(a,b) present the magnitude of the systematic velocity error,  $u'_s = \sqrt{(u'_s)_x^2 + (u'_s)_y^2 + (u'_s)_z^2}$ , where Figure 15a plots the absolute error in units of  $mm/s$ , and Figure 15b is the relative error, expressed as a percentage of the local time- and depth-averaged velocity ( $u'_s/\bar{u}$ ). (Note that hereafter the angle brackets,  $\langle \cdot \rangle$ , denote the spatial averages of the error, which are given on top of some plots to express its overall magnitude.) The regions of higher errors, ranging from 0.3 to 1  $mm/s$  are located at the edges of the cavity (along the walls) and in the mixing layer. However, when divided by the local time-averaged velocity, these errors become negligibly small ( $< 1\%$ ).

Note that to avoid division by zero/very small values in the calculation of relative error, the velocity data was filtered. The filter threshold was set to 0.4 and 0.6  $mm/s$  for the  $U_\infty = 0.13$  and 0.19  $m/s$  cases, respectively. (These were chosen so that 95% of the data had a relative velocity error less than 5%.) These values determine the sensitivity of the measurement method, thus, the experimental data would be similarly filtered.

As was already clear from Figure 12c, the systematic error in the vertical direction is much larger than that in the horizontal direction. Therefore, one expects the total velocity error also to be dominated by its vertical component. Thus, the velocity error in the vertical direction must be further quantified. The magnitude of the vertical velocity error,  $(u'_s)_z$ , is presented on Figure 15c, along with its relative value,  $(u'_s)_z/\bar{u}_z$ , (Figure 15d). These plots show that the vertical error can reach 1  $mm/s$  or 20% of the local velocity in some regions, which primarily correspond to zones of small vertical velocity. Nevertheless, 96% of the data has a systematic error of less than 5% of the local vertical velocity.

The total random velocity error,

$$u'_r = \sqrt{(u'_r)_x^2 + (u'_r)_y^2 + (u'_r)_z^2}, \quad (21)$$

given on Figures 16a,b, is smaller than the systematic error; the spatially averaged value decreases from 0.23 to 0.10 mm/s. Again, this indicates that unsteady surface disturbances are not the dominant source of error in this work. Note that the random velocity error is also dominated by its vertical component,  $(u'_r)_z$ , (Figure 16c,d), its space average is 0.08 mm/s compared to the total 0.10 mm/s. However, relative to the local mean vertical velocity,  $(u'_r)_z/\bar{u}_z$ , it is still within acceptable limits (Figure 16d).

Overall, the total velocity error, calculated as the sum of its random and systematic components, is 0.16 mm/s for the case of no surface gravity waves and 0.22 mm/s for the case with waves. Although the surface waves increase the absolute error by 35%, as the average velocities for this case are larger, and the relative velocity error decreases from 0.4% to 0.3% of the average velocity of the gyre in the cavity (see Section 4). Both the systematic and random velocity errors are dominated by their vertical components (because the camera angles are small, 7.5°, and the vertical uncertainty is expected to be much larger than the horizontal one, see Figure 7). Nevertheless, after normalizing (relatively large) vertical velocity errors with (relatively low) vertical velocities, the errors are below 5% for 96% of the data.

This method of error analysis allows for the calculation of the spatial distributions of both systematic and random errors in velocity measurements. From Figure 12c and additional graphs not shown here (see Akutina, 2016), it is clear that the regions near the walls of the cavity have a large systematic error, most likely due to surface tension effects. Thus, it is reasonable to exclude the region within 5 mm from the walls from subsequent analyses. There is often a region of (relatively) larger error in the shear layer. However, the error within that region is nevertheless acceptable (< 5%).

We note, however, that the error analysis of this method does not capture the variation of the position error in the vertical direction,  $\frac{\partial r'}{\partial z}$ , and the errors that appear in the later stages of the PTV analysis. To address these two issues, the second method of error analysis was developed and implemented.

### 3.3.2 Velocity errors - Method 2: “Dumbbell”

To calculate the velocity measurement uncertainty of a PTV (or a PIV) system, it is desirable to conduct a test in which the exact velocities of the tracking points are known. One of the common methods is to measure the velocities of points on a rotating disk (see, for example, Weitbrecht et al, 2002). However, this method is not ideal for the current set-up primarily because of the imaging through the free surface. In a rotating-disk test, the points always move on the same circular trajectories, whereas from the previous section it is clear that the velocity error at a point depends on the direction in which the particle is moving, as it will go through different regions of the position error field. Also, the rotating disk is flat and will again be insensitive to the vertical derivative of the position error. A complex, three-dimensional object could have been constructed, but in that case it would have been impossible to rotate it inside the cavity without creating significant disturbances to the flow.

An alternate way of testing the quality of the velocity measurements that is more suitable to the experimental conditions is therefore required. There exists a well-known camera calibration technique for PTV systems called dynamic calibration or a “dumbbell” calibration (Gülan et al, 2012). In the dumbbell calibration, two points, separated by a fixed distance, are moved within the domain of interest. The calibration parameters are then optimized while maintaining the

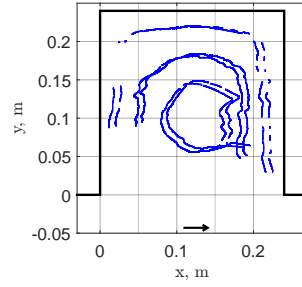


Fig. 17: Example of the trajectories of the 2 particles on the dumbbell target,  $U_\infty = 0.13$  m/s.

separation distance. In this study, this method is extended to the assessment of velocity errors by recognizing that two particles with a constant separation distance must also have zero relative velocity along the vector that connects them. A dumbbell was created by glueing two particles (polyethylene microspheres 212-250  $\mu\text{m}$  in diameter, the same as those used for the PTV experiments) onto a piece of black plastic with a separation distance of 9.36 mm. (The separation distance was calculated as the average distance,  $\bar{d}$ , between the particles measured during the experiments described below.) A thin handle was attached to the dumbbell to allow it to be moved within the measurement domain (see Akutina, 2016, for details).

The error estimation was made by recording the trajectories of the two particles on the dumbbell as the latter was moved within the cavity in a manner that followed the streamlines and approximated the velocities therein. Images were recorded for the two flow cases, with and without surface gravity waves, over a 30 s duration (to mimic the velocity errors of the experiments). The imposed motion also had a vertical component to be able to estimate  $\frac{\partial v'}{\partial z}$ . An example of the measured dumbbell trajectory is given in Figure 17. After discarding the data in which one of the dumbbell points was not visible, 23 seconds of data remained for  $U_\infty = 0.13$  m/s case and 14 seconds for  $U_\infty = 0.19$  m/s case.

The recordings were post-processed using the same procedure as the actual experiments (Section 2), and the measured distance between the two particles,  $d$ , was calculated as:

$$d(t) = \sqrt{(x_2 - x_1)^2 + (y_2 - y_1)^2 + (z_2 - z_1)^2},$$

where  $x$ ,  $y$ , and  $z$  are the coordinates of the particles. The distance between the points is constant, so the standard deviation of  $d(t)$  gives us an estimation of the position error of the system.

The velocity of the two dumbbell particles towards or away from each other was calculated as the scalar projection of the relative velocity between two particles,  $(\mathbf{u}_1 - \mathbf{u}_2)$ , onto the vector,  $\mathbf{k}$ , connecting them:

$$u_{1,2} = \frac{(\mathbf{u}_1 - \mathbf{u}_2) \cdot \mathbf{k}}{|\mathbf{k}|}.$$

The deviation of  $u_{1,2}$  from zero is then a measure of velocity error in the experiment.

Figure 18 shows the probability density functions (PDFs) of the difference between the measured and the true  $d(t)$  for the two flow cases, whose standard deviations are 0.011 and 0.012 mm for the cases with no waves and with waves, respectively. In the previous test (with the stationary pattern) the total position ambiguity (systematic plus random) was 0.32 mm and 0.38 mm under the same conditions. The relative position error between closely spaced points (10 mm

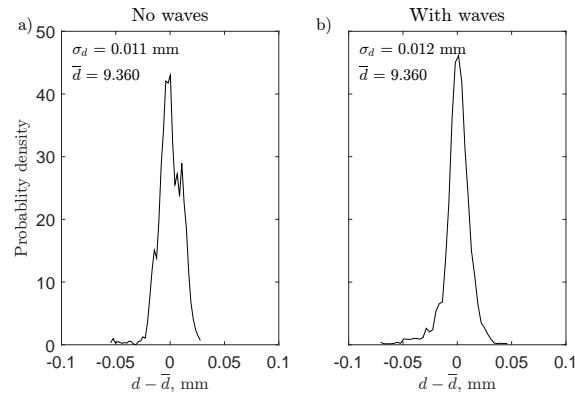


Fig. 18: Empirical PDFs of the distance,  $d(t)$ , between the two particles on the dumbbell target. a)  $U_\infty = 0.13$  m/s. b)  $U_\infty = 0.19$  m/s.

in the dumbbell) is therefore more than an order of magnitude smaller than the maximum absolute position error. This explains why it is possible to get quite accurate velocity measurements even with relatively large absolute position errors (0.3-0.4 mm).

Figure 19 presents the probability density functions of  $u_{1,2}(t)$ , whose standard deviation is  $0.39$  mm/s without waves and  $0.68$  mm/s with waves. This is larger than the errors obtained from the stationary dot pattern whose errors were  $0.16$  mm/s and  $0.22$  mm/s, respectively. This difference is mainly attributed to the polynomial fit procedure (used to calculate velocities along the lagrangian particle trajectory), which was not accounted for in the first tests. This explanation is confirmed by the observation the error magnitudes in the dumbbell test trajectories increased at the trajectory ends, where the polynomial fit deteriorates. In addition, a larger error in the polynomial fit occurs since the trajectories of the dumbbell were considerably less smooth (being moved by hand) than for PTV particles advected by the flow. Thus, even though, these velocity errors are somewhat overestimated, we have demonstrated that they are nevertheless small, less than  $1$  mm/s (or  $1 - 3\%$  of the average velocity in the domain, and less than  $0.4\%$  of  $U_\infty$ ).

It can be noted that future work could involve moving the dumbbell using a 3D traversing mechanism (rather than manually) to avoid additional vibrations. Also, if the flow under consideration is contained in a closed chamber, one could consider making the dumbbell out of a neutrally buoyant material so that it could be advected by the flow.

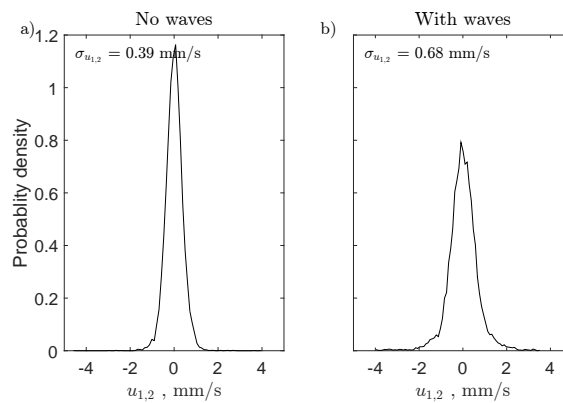


Fig. 19: Empirical PDFs of the projection of the relative velocity on the separation vector between two points on the dumbbell target,  $u_{1,2}$ . a)  $U_\infty = 0.13$  m/s. b)  $U_\infty = 0.19$  m/s.

Table 2: Summary of all the position errors calculated and measured in this work: i) from the experiment with the stationary pattern (Method 1), ii) using the dumbbell target (Method 2), iii) due to the unsteady interface calculated theoretically in Section 3.1.1, iv) due to calibration imperfections measured in still water (Section 3.2).

Quantity	$U_\infty$ , mm/s	Position error, mm					
		Absolute Stationary pattern test			Relative Dumbbell test	Due to variable interface (Section 3.1.1)	Due to calibration; in still water (Section 3.2)
		Systematic	Random	Total	Total		
x	130	0.11	0.01	0.12		0.04	0.03
	190	0.07	0.03	0.10			
y	130	0.06	0.01	0.07		0.04	0.03
	190	0.09	0.03	0.12			
z	130	0.23	0.07	0.30		0.30	0.20
	190	0.16	0.18	0.34			
r	130	0.26	0.07	<b>0.32 (1.1% of H)</b>	<b>0.011 (0.04% of H)</b>	<b>0.30</b>	<b>0.20</b>
	190	0.20	0.18	<b>0.38 (1.2% of H)</b>	<b>0.012 (0.04% of H)</b>		

Table 3: Summary of the velocity errors obtained from two error analysis experiments: i) with the stationary pattern (Method 1), and ii) with the dumbbell target (Method 2).  $U_\infty$  is the free-stream velocity, and  $\langle \bar{u} \rangle = \langle \bar{u}(x,y,z) \rangle$  is the average velocity in the domain (overbar denotes time averaging, while angle brackets correspond to spatial averaging).

Quantity	$U_\infty$ , mm/s	Velocity error, mm/s			
		Stationary pattern test			Dumbbell target test
		Systematic	Random	Total	Total
$u_x$	130	0.18	0.01	0.19	
	190	0.12	0.03	0.15	
$u_y$	130	0.10	0.005	0.10	
	190	0.08	0.02	0.10	
$u_z$	130	0.32	0.03	0.35	
	190	0.17	0.09	0.26	
u	130	0.38	0.03	<b>0.41 (0.3% of <math>U_\infty</math> or 1.1% of <math>\langle \bar{u} \rangle</math>)</b>	<b>0.39 (0.3% of <math>U_\infty</math> or 1.1% of <math>\langle \bar{u} \rangle</math>)</b>
	190	0.23	0.10	<b>0.33 (0.2% of <math>U_\infty</math> or 0.5% of <math>\langle \bar{u} \rangle</math>)</b>	<b>0.68 (0.3% of <math>U_\infty</math> or 1.1% of <math>\langle \bar{u} \rangle</math>)</b>

## 4 Discussion

### 4.1 Position error

Given that the optimal camera angle was used ( $7.5^\circ$  here), position errors arising from an unsteady optical interface were first calculated theoretically. For the maximum angle of  $0.2^\circ$  and maximum interface elevation of 1 mm, the errors were 0.04, 0.04 and 0.3 mm in the  $x$ -,  $y$ -, and  $z$ -directions, respectively. (See the summary in Table 2.) This is slightly larger than the average random component of the position error estimated using Method 1 – the stationary dot pattern (0.03, 0.03 and 0.18 mm). The measured error is presumably lower than the theoretically predicted one given that the latter calculation used maximum surface angles whereas the former resulted from the whole range of surface disturbances (large and small).

The errors due to imperfections of the stereoscopic model alone are 0.03, 0.03 and 0.2 mm in the  $x$ -,  $y$ -, and  $z$ -directions, respectively, which is almost the same as the measured errors due to the waves (0.03, 0.03 and 0.18 mm). Also, the systematic component of the error is consistently larger than the random component for both the cases with and without gravity waves, suggesting that the contribution of the error from the surface disturbances is relatively small. The absolute total position error measured is 0.32 mm or 1.1% of  $H$ , for the case of no waves and 0.38 mm or 1.2% of  $H$  for the case of strong surface gravity waves, a difference of only 15%, suggesting that the contribution of the wavy surface to the total error is again not very large. (Recall that  $H$  here is the maximum distance from the interface to the measurement plane, which in our case is the same as the water depth,  $h$ , since the measurements are performed in the entire water column.) The relative position error determined by the dumbbell method is 30 times smaller than the absolute error at 0.011 mm for no waves and 0.012 mm with waves, corresponding to 0.04% of  $H$ . It is important to note that the separation distance between the two points on the dumbbell should be chosen to be greater (or equal to) the maximum displacement of a particle per frame in the given flow field in order to be representative of the relative position error experienced by the particle during one time step. In this work, the separation distance is much larger than the particle displacement, so the relative position errors are possibly even smaller than what is estimated.

#### 4.2 Velocity error

The velocity error is similar for the cases with and without gravity waves (Table 3). The error is smaller when the gravity waves are present (0.33 mm/s or 0.5% of the average velocity in the domain for  $U_\infty = 0.19$  compared to 0.41 mm/s or 1.1% of the average velocity for  $U_\infty = 0.13$ ). This is attributed to the fact that near-wall data was not available for the case with the higher free-stream velocity, so that the error associated with surface tension effects was underestimated. The random component of the error is larger for the case with surface waves, however it remains smaller than the systematic error.

The vertical velocity error is about two to three times larger than the horizontal ones for both cases (with and without waves). This difference is clearly due to the geometrical arrangement of the stereoscopic system, *i.e.* the small angle between the cameras, and this difference does not change with increasing surface curvature.

## 5 Conclusions

The errors associated with optical measurements made through an unsteady optical interface were investigated. The main results can be summarized as follows.

An analytical estimation of the *i*) optimum camera angle with respect to the variable interface, and *ii*) the resulting position errors as a function of the interface displacement and inclination are obtained. The estimated position errors agree with those measured in the current experimental configuration. Practical information about the optimum camera angles for particular values of surface perturbations can be obtained from Figure 9.

Two methods of measuring velocity errors were proposed. These methods can be applied to setups where an unsteady optical interface is present, such as a stratified flow with internal gravity waves, a flow with shock waves, or free-surface

flows such as the one presented herein. Also, these methods can be used to quickly assess the uncertainties in a setup with no additional optical disturbances.

In the first method, a planar pattern was used to measure the position errors due to the variable optical interface. For a relatively isotropic flow the velocity error can be quickly estimated by taking the spatial derivative of this field and ensuring that  $\frac{\partial \mathbf{r}}{\partial \mathbf{x}_j}$  is less than a critical value (*e.g.* 5%). If the flow is highly anisotropic and heterogeneous the full test will provide the spatial variability of the velocity error. Either way, a quick and simple test to check the quality of the velocity measurements is the second method, the “dumbbell” test, where a small rod with two particles glued onto it is tracked by the optical system; the deviation from zero of the relative velocity of these two particles along the vector connecting them should be small.

These methods of error assessment can be applied to 2D and 3D optical measurements methods (PTV and PIV). For PIV where a correlation method is used on a group of particles, a particle cloud can be glued onto the ends of the dumbbell.

To the authors’ knowledge, 3D-PTV through an unsteady interface had never been performed prior to this work. Large errors were thus expected from the changing angles of refraction of the unsteady wavy surface through which particles are tracked. As a result of this work, it appears that if the waves are slow and long compared to the flow velocity, it is relatively straightforward to obtain accurate velocity measurements.

This finding can be quite influential in the field of environmental fluid mechanics, where it is often not possible to take data through a glass wall (for example, wide channels with sediments on the bottom) and the only accessible surface is the free surface. In these cases, only surface data is usually obtained (by way of floating particles). A similar problem is faced when internal gravity waves are present at an interface between two media.

In summary, although the absolute positions to which the velocity vectors are assigned is distorted by the unsteady interface, the magnitude of the velocity vectors themselves remains accurate as long as the waves are slowly varying (have low curvature). To estimate the optimum camera angles the maximum slope and amplitude of the unsteady interface should be considered. These two parameters will also determine the position distortion in the measurements. However, the velocity errors are solemnly determined by the rate of change of the surface properties (of slope and elevation) in space and time. Clearly, the stronger the disturbances on the interface are (high amplitude, short wave length), the smaller is the distance from the interface at which the measurements can be performed.

We have demonstrated that measurements should not be immediately deemed infeasible when distortions due to surface waves are visible. We have observed that optical measurements are considerably more robust when subjected to such distortions than one would have initially thought.

## 6 Acknowledgement

The authors would like to thank John Bartczak for his invaluable help with the laboratory experiments.

## References

- 1  
2 Akutina Y (2016) Experimental investigation of flow structures in a shallow embayment using 3D-PTV. PhD thesis,  
3 McGill University, Canada (escholarship.mcgill.ca), URL <http://digitool.library.mcgill.ca/R/>  
4  
5 Elsinga G, Orlicz G (2015) Particle imaging through planar shock waves and associated velocimetry errors. *Experiments*  
6 *in Fluids* 56(6):1–12  
7  
8 Fincham A, Spedding G (1997) Low cost, high resolution dpiv for measurement of turbulent fluid flow. *Experiments in*  
9 *Fluids* 23(6):449–462  
10  
11  
12 Gülan U, Lüthi B, Holzner M, Liberzon A, Tsinober A, Kinzelbach W (2012) Experimental study of aortic flow in the  
13 ascending aorta via particle tracking velocimetry. *Experiments in Fluids* 53(5):1469–1485  
14  
15 Levin I, Savchenko V, Osadchy V (2008) Correction of an image distorted by a wavy surface: laboratory experiment.  
16 *Applied Optics* 47(35):6650–6655  
17  
18 Lüthi B, Tsinober A, Kinzelbach W (2005) Lagrangian measurement of vorticity dynamics in turbulent flow. *Journal of*  
19 *Fluid Mechanics* 528:87–118  
20  
21  
22 Maas H, Gruen A, Papantoniou D (1993) Particle tracking velocimetry in three-dimensional flows. *Experiments in Fluids*  
23 15(2):133–146  
24  
25 Malik N, Dracos T, Papantoniou D (1993) Particle tracking velocimetry in three-dimensional flows. *Experiments in*  
26 *Fluids* 15(4-5):279–294  
27  
28 Morris NJ, Kutulakos KN (2005) Dynamic refraction stereo. In: *Proceedings of the 10th International Conference on*  
29 *Computer Vision, IEEE*, pp 1573–1580  
30  
31  
32 OpenPTV-Consortium (2014) Open source particle tracking velocimetry. URL [www.openptv.net](http://www.openptv.net)  
33  
34 Richard H, Raffel M (2001) Principle and applications of the background oriented schlieren (BOS) method. *Measurement*  
35 *Science and Technology* 12(9):1576–1585  
36  
37 Tian Y, Narasimhan SG (2009) Seeing through water: Image restoration using model-based tracking. In: *Proceedings of*  
38 *the 12th International Conference on Computer Vision, IEEE*, pp 2303–2310  
39  
40  
41 Weitbrecht V, Kühn G, Jirka G (2002) Large scale piv-measurements at the surface of shallow water flows. *Flow Mea-*  
42 *surement and Instrumentation* 13(5):237–245  
43  
44 Westerweel J (2000) Theoretical analysis of the measurement precision in particle image velocimetry. *Experiments in*  
45 *Fluids* 29(1):3–12  
46  
47 Willneff J (2003) A spatio-temporal matching algorithm for 3d particle tracking velocimetry. PhD thesis, Swiss Federal  
48 Institute of Technology (ETH) Zurich, Switzerland  
49  
50  
51  
52  
53  
54  
55  
56  
57  
58  
59  
60  
61  
62  
63  
64  
65